A high-fidelity multiresolution DEM model for Earth systems

Duan Xinqiao[1], Li Lin[1, 2, 3], Zhu Haihong[1, 3], Ying Shen[1, 3]

[1]Geographical Information Science Faculty, SRES School, Wuhan University, Wuhan, 430079, China
[2]Geospatial information science Collaborative Innovation Centre of Wuhan University, Wuhan, 430079, China
[3]The Key Laboratory for Geographical Information System, Ministry of Education, Wuhan, 430079, China

Correspondence to: Li Lin (lilin@whu.edu.cn)

Abstract. The topographic impacts on modifying Earth systems variability have been well recognised. As numerical simulations evolved to incorporate broader scales and finer processes, accurately embedding the underlying topography to simulate land – atmosphere – ocean interactions, or performing commensurate scale transformation to topography while considering high-fidelity retention have proven to be quite difficult. Numerical schemes from Earth systems either use empirical parameterization as sub-grid scale and downscaling skills to express topographic endogenous processes, or rely on insecure point interpolation to induce topographic forcing, which create bias and input uncertainties. DEM generalisation provides systematic topographic transformation by considering loyal fidelity, but existing heuristic approaches are not performed optimally because of point clustering, or are difficult to incorporate into numerical systems because of sliver triangles. This article proposes a novel high-fidelity multiresolution DEM model with high-quality grids to meet the challenges of scale transformation. The generalised DEM model is initially approximated as a triangulated irregular network (TIN) via selected terrain feature points, control points, and possible embedded terrain features. The TIN surface is then optimized through an energy-minimized centroidal Voronoi tessellation (CVT). By devising a robust discrete curvature as a density function and exact geometry clipping as an energy reference, the developed curvature CVT (cCVT) converges, the generalised model evolves to a further approximation to the original DEM surface, and the points and their dual cells become equalized with the curvature distribution, exhibiting a quasi-uniform high-quality grid. The cCVT model is then evaluated on real LiDAR-derived DEM datasets compared to the classical heuristic method. The experimental results show that the cCVT multiresolution model outperforms classical heuristic DEM generalisations in terms of both surface approximation precision and surface morphology retention.

1 Introduction

1.1 Topography in Earth systems

Topography is one of the main factors controlling processes operating at or near the surface layer of the planet (Florinsky and Pankratov, 2015; Wilson and Gallant, 2000). With the success of Earth and environment systems with these scale diversified processes, there exists persistent demands for extending their utility into new and expanding scopes (Ringler et al., 2008; Tarolli, 2014; Wilson, 2012), as exemplified by lapse-rate controlled functional plant distributions (Ke et al., 2012),

orographic forcing imposed on oceanic and atmospheric dynamics (Nunalee et al., 2015; Brioude et al., 2012; Hughes et al., 2015), topographic dominated flood inundations (Bilskie et al., 2015; Hunter et al., 2007), and many other geomorphological (Wilson, 2012), soil (Florinsky and Pankratov, 2015), and ecological (Leempoel et al., 2015) examples from Earth systems. However, as numerical simulation systems evolved to incorporate broader scales and finer processes to produce more fidelity predictions (Ringler et al., 2011; Weller et al., 2016; Wilson, 2012; Zarzycki et al., 2014), how to accurately embed the topography with finer resolution, or how to perform commensurate scale transformation to the topography have proven to be a quite difficult task (Bilskie et al., 2015; Chen et al., 2015; Tarolli, 2014).

Earth and environmental simulations usually adopt sub-grid scheme to exert topographical heterogeneity and rely on downscaling the finer observations to surface variables (Fiddes and Gruber, 2014; Kumar et al., 2012; Wilby and Wigley, 1997). Coupled or assimilated observations construct a reasonable base for dynamic or statistical downscaling. However, the observations themselves are always of confined resolution, whilst sub-grid scheme are designed for the empirical parameterization rather than intrinsic feature capturing, which implies bias of endogenous variability and mixed-up uncertainties in grid cells (Jiménez and Dudhia, 2013; Nunalee et al., 2015). The topography are also commonly treated as a static boundary layer in dynamics simulations, where different interpolation strategies and mesh refinement skills are used to convey terrain variation (Guba et al., 2014; Kesserwani and Liang, 2012; Nikolos and Delis, 2009; Weller et al., 2016). However, mesh from interpolated vertices does not necessarily comply with the terrain relief, and bed elevation errors are frequently reported as one input uncertainty (Bilskie and Hagen, 2013; Hunter et al., 2007; Nunalee et al., 2015; Wilson and Gallant, 2000). While there are many situations where dynamic conditions are stressed for stronger impacts on modifying predictions (Cea and Bladé; Budd et al., 2015), but the underlying topography is still prominently important for its increasingly improved fidelity to the Earth's surface (Bates, 2012; Tarolli, 2014), and a sophisticated topography transformation would be beneficial to reduce discrepancies arisen from physical inconsistencies (Chen et al., 2015; Glover, 1999; Ringler et al., 2011).

1.2 Multiresolution DEM model

Systematic scale transformation of topographic data has long been studied under terrain generalisation, where precise surface approximation and terrain structural feature retention have both been pursued (Ai and Li, 2010; Chen et al., 2015; Guilbert et al., 2014; Jenny et al., 2011; Weibel, 1992; Zhou and Chen, 2011). Triangulated irregular networks (TIN) are generally chosen as a substitute for the regularly spaced grids (RSG), and critical points or salient points with terrain significance are selected for the network feature points. Triangular networks are used for their adaptiveness to a locally enhanced multiresolution scheme. Critical points or salient points are selected because they can effectively improve the approximation precision (Heckbert and Garland, 1997; Zakšek and Podobnikar, 2005; Zhou and Chen, 2011).

As surface approximation precision and terrain feature retention are competitive for the redistribution of feature points, DEM (digital elevation model) generalisation is differentiated from terrain generalisation for its emphasis on surface approximation as a whole, with the aim of providing precise surface interpolation (Guilbert et al., 2014). Terrain

generalisation emphasises geomorphology or landform depiction where map cognitive efforts are drawn to produce progressive data reduction, with the effects that the main relief features strongly stressed while non-structural details are massively suppressed (Ai and Li, 2010; Guilbert et al., 2014; Jenny et al., 2011). Since the static topographic layer are commonly composed directly by DEM datasets to diverse simulation interests, maintaining precise surface approximation for rigorous boundary conditions is more important than 'sparse' geomorphology representation. While DEM datasets are usually used interchangeably with topography or terrain in Earth systems, we will use DEMs and topography indiscriminately hereafter.

Existing DEM generalisation can be roughly catalogued into two groups, namely, heuristic refinements and smooth fitting, according to differences in the surface approximation strategy. The first class of approaches is due to the computational bottleneck consideration, that determination which combination of vertices to a TIN surface approximates the original dense DEM surface best needs exponential time (Chen and Li, 2012; Heckbert and Garland, 1997). It thus forces existing methods to employ some heuristic strategy, which adopts greedy insertion refinements (or deletion) on feature points, to find a sub-optimal approximation solution that is computationally practical. In each insertion (or deletion), rearranging the entire existing grid to obtain a better approximation is also computationally inhibitive and thus not adopted (Chen et al., 2015; Heckbert and Garland, 1997; Lee, 1991), and this may result in the clustering of feature points. Among those existing heuristic approaches, trenching the pre-extracted terrain features (drainage streamlines for example) into the TIN surface seems quite appealing (compound method) (Chen and Zhou, 2012; Zhou and Chen, 2011), but the quality of the generalised TIN surface cannot be guaranteed, and the existence of thin sliver triangles makes it difficult to be incorporated with numerical stability (Kim et al., 2014; Weller et al., 2009). The second class of approach is due to the consideration of TIN surface from feature points do not necessarily warrants best approximation to the original dense DEM, for feature points are commonly selected through some local metric. Many researches thus considered surface approximation globally instead of elaborated feature point selection, such as bi-linear, bi-quadric, multi-quadric, Kriging, or general radial base function-based fittings (Aguilar et al., 2005; Chen et al., 2015; Schneider, 2005; Shi et al., 2005). The proposed multi-quadrics (Chen et al., 2012; Chen et al., 2015), for example, approximates the original DEM surface well with a high-order smooth surface and the smooth surface provides a kind of weeding mechanism to cure the feature point clustering problem. But the high-order radial base function is computational expensive when a broad scenario is involved (Chen et al., 2015; Mitášová and Hofierka, 1993). In brief, existing DEM transformations are neither best performed with loyalty to the original terrain surface, nor easily incorporated by the numerical schemes.

1.3 Aims and contributions

The purpose of this article is to devise a multiresolution DEM model that considers optimized surface approximation and guaranteed grid quality. The quality grid is demanded by the aforementioned easy incorporation with the simulation systems. Multiresolution is an effective paradigm to model scale diversity (Du et al., 2010; Guba et al., 2014; Ringler et al., 2011; Weller et al., 2016), among those promising plans, we are especially fascinated by the centroidal Voronoi tessellations

(CVTs) method for the intuitive way to redistribute samples with a designated function (Du et al., 1999; Du et al., 2010; Ringler et al., 2011), and develop CVT to an optimized surface transformation method to realize multiresolution terrain model.

CVT is essentially a two-stepped optimization loop, i.e., spatial domain equalization from Voronoi tessellation and property domain equalization from barycentre computation (Du et al., 1999). To make this general-purposed optimization tool work for DEM transformation, we made a few contributions as follow:

(1) The generalised DEM surface is initially approximated by a triangular grid (TIN) constructed from selected feature points. The selection of feature points have important morphological structures embedded, computed (such as D8 flow algorithm) or auxiliary input morphological lines have been proved to have significant influence on the quality of transformed DEM surface (Zhou and Chen, 2011). The proposed method keeps the structural lines in the optimization loop and makes it different to existing CVT implementations where stationary points are commonly not considered.

(2) For the discrete TIN surface, we compute robust mean curvature as incident property. Upon this discrete spatial domain and property domain, the CVT loops and make discrete set equalized from both domains. Spatial equalization warrants a quasi-uniform quality TIN grid, while the intrinsic property domain equalization warrants distribution of the discrete facets conforms to inherent terrain variation. It thus a total different approach to DEM generalisation and we called it curvature CVT (cCVT).

(3) Existing CVT implementation often undertake clustering approach. However, clustering over discrete sets suffers from numeric issues such as zigzag boundaries, invalid cluster cells (Valette et al., 2008), and limited grid quality. By devising an exact geometry clipping technique, this article develops a dedicated CVT algorithm for DEM transformation which helps to improve or avoid the numeric problems above.

The cCVT works on discrete set, but has global optimization mechanism. It promises an optimized surface approximation and quality grid, which build a high-fidelity multiresolution terrain model. From this terrain model reliable surface variables can be estimated under a coupled system, or computational mesh can be constructed and refined to possible dynamic conditions.

1.4 Organization of the article

The rest of the article is organized as follows. In Section 2 the theory behind CVT for optimized DEM surfaces is introduced, techniques for incorporating DEM generalisation principles and fast convergence are presented, and the differences between the cCVT implementation and classical clustering approach are discussed. In Section 3, the cCVT model is tested with real LiDAR-derived terrain datasets. Section 4 discusses some considerations, comparable results, possible causes, and interpretations of the cCVT model. Finally, Section 5 presents short conclusion and outlooks briefly.

2. Curvature centroidal Voronoi tessellation on DEM surface

2.1 Definition

Centroidal Voronoi tessellation is a space tessellation for each Voronoi cell's geometrical centre (in the spatial domain) that coincides with its barycentre from the abstract property domain (Du et al., 1999). Here, the property domain is analogous to the frequency domain. For the vertices set t $\{v_i\}_k^1$ in $\Omega \subset R^3$, the Voronoi tessellation graph is defined as:

$$V_i = \{p \in \Omega: |p - z_i| < |p - v_j|, j = 1..k, j \neq i\}, \mathrm{i} = 1..\mathrm{k}., \quad (1)$$

That is, a Voronoi cell V_i is the set of points whose distance to $\boldsymbol{v_i}$ is less than that to any other vertices. $|\cdot|$ is the Euclidean norm. Every vertex and its corresponding dual cell commonly have some intensity scalar $\boldsymbol{\rho}$ attached from some abstract property domain, which is called a density function. The total potential energy of the Voronoi graph $\boldsymbol{V}$ of a terrain surface can be computed by summing up every cell $\boldsymbol{V_i}$'s potential energy:

$$E = \sum_{i=1}^{k} \iint \rho \cdot |p - v_i|^2 \cdot d\sigma, \quad (2)$$

Energy minimizer:

$$\bar{x} = \frac{\iint x \cdot \rho \cdot d\sigma}{\iint \rho \cdot d\sigma}; \ \bar{y} = \frac{\iint y \cdot \rho \cdot d\sigma}{\iint \rho \cdot d\sigma}; \bar{z} = \frac{\iint z \cdot \rho \cdot d\sigma}{\iint \rho \cdot d\sigma}, \quad (3)$$

which minimizes the surface's total potential, for $\overline{v_i} = (\bar{x}, \bar{y}, \bar{z})$ satisfies:

$$\frac{\partial E}{\partial p} = 2(p - v_i) \cdot \iint \rho \cdot d\sigma = 0 \ , \quad (4)$$

In other words, when $\boldsymbol{v_i}$ coincides with the barycentre $\overline{\boldsymbol{v}_i}$, each cell's potential effect on the property domain (gravity) becomes equalized to a stable energy state.

2.2 Lloyd Relaxation

The most classical energy minimization process of centroidal Voronoi tessellation is expressed by *Lloyd's Relaxation* (Lloyd, 1982). The main idea of this algorithm is to first tessellate the surface; density integration over the area is then performed to find a 'gravity' barycentre for each tessellated cell, which is used as the new site for the iteration. The pseudo code of this procedure is shown below:

Algorithm1 Lloyd_relaxation
Inputs: vertices set $\boldsymbol{N} = \{\boldsymbol{v_i}\}_{\boldsymbol{k}}^{\boldsymbol{1}}$

while ($\Delta \boldsymbol{E} > \boldsymbol{Threshold}$*)*
{
  use the ***k*** *vertices to tessellate the surface, obtain Voronoi cells* ***{Vi};***
  clear ***N*** *;*

  for each ***Vi*** *in* ***{Vi}***
  {

Compute barycentre of $\boldsymbol{V_i}$: $\bar{\boldsymbol{x}} = \frac{\iint \boldsymbol{x}\cdot\boldsymbol{\rho}\cdot d\boldsymbol{\sigma}}{\iint \boldsymbol{\rho}\cdot d\boldsymbol{\sigma}}$; $\bar{\boldsymbol{y}} = \frac{\iint \boldsymbol{y}\cdot\boldsymbol{\rho}\cdot d\boldsymbol{\sigma}}{\iint \boldsymbol{\rho}\cdot d\boldsymbol{\sigma}}$; $\bar{\boldsymbol{z}} = \frac{\iint \boldsymbol{z}\cdot\boldsymbol{\rho}\cdot d\boldsymbol{\sigma}}{\iint \boldsymbol{\rho}\cdot d\boldsymbol{\sigma}}$;

push $(\bar{\boldsymbol{x}}, \bar{\boldsymbol{y}})$ *to* $\boldsymbol{N}$*;*

}

compute $\boldsymbol{E}$*;*

}

We follow Lloyd's elegant idea. The barycentre of a 2-dimentional Voronoi cell may fall outside this surface patch, so an additional calculation may be needed to amend this. Du et al. suggested to project the barycentre onto a nearest facet and the constrained projection point is used instead for the new sites (Du et al., 2003). Others suggest quadric interpolations over all the facets of the cluster for further accurate site calculation (Valette et al., 2008).

2.3 Fast converge to DEM equilibriums

2.3.1 Clustering CVTs

Lloyd's Relaxation requires Voronoi tessellation on a discrete 2-dimensional surface, but direct Voronoi tessellation on a piece-wise smooth surface requires costly geodesic computation and may be challenged by complicated numerical issues (Cabello et al., 2009; Kimmel and Sethian, 1998)， Du et al. suggested that CVT could be realized through some clustering approaches (Cohen-Steiner et al., 2004; Du et al., 1999; Du et al., 2003), that is, using the attached property as density function to cluster facets and then find the clustered cells' barycentres to create new clustering sites. Through this heuristic iteration, the new sites along with the new tessellations compose better and better approximation to the original surface, with their spatial distribution conforms to the pre-defined density function.

The clustering approach avoids geodesic tessellation by direct facets combination, which is computationally light. The greatest expenditure then comes from global distance computation for identifying every cell to its cluster centre. However, this *k-means* like clustering over discrete facets suffers from some numeric issues concerning Voronoi cells such as zigzag boundaries – since no geodesic Voronoi tessellation used, and invalid clusters due to disconnected set of facets (Valette and Chassery, 2004; Valette et al., 2008). The keys to the quick clustering algorithm lies in that, it avoids generating new sites (to avoid surface reconstruction) and relies on existing sites (or facets). Thus, the generated grid may not be well qualified.

2.3.2 Curvature as density function

Terrain surface critical points such as peaks, pits, and saddles are treated as gravity equilibria and key elements depicting the surface geometry in the large (Banchoff, 1967; Milnor, 1963); a further extended critical points on a second-order surface derivative (such as curvature) will describe a more detailed set of terrain surface parameters (Jenny et al., 2011; Kennelly, 2008). When constructing a generalised DEM surface, these feature points are commonly used as a base set, and additional input points, or pre-extracted terrain structures are embedded for further approximation (Guilbert et al., 2014; Zakšek and Podobnikar, 2005; Zhou and Chen, 2011). The additional input points or pre-extracted terrain structures of interest are also commonly required in numerical simulation setups for cross-checking or validation purposes.

Based on these observations, and consider requirements of the CVT variational framework, this article proposes a feature points based scheme (including boundary points, feature points, and pre-extracted structural points of interest) as initial Voronoi sites. For optimized spatial distribution of these sample points, we calculate a robust discrete mean curvature as density function, which is based on the recognition of curvature's flexibility on capturing shape characteristics and capability conducting shape evolution (Banchoff, 1967; Kennelly, 2008; Pan et al., 2012). Curvature's flexible ability on depicting terrain morphology has been appreciated by many researches. For example, P. J. Kennelly pointed out that, compared to the result of flow accumulation model, curvature based delineation of drainage networks has not limit to one pixel thickness and requires no depression filling (Kennelly, 2008). The robust discrete curvature calculation is referred to *Meyer et al.* (2003).

2.3.3 Improved CVT implementation from approximation

The *Lloyd Relaxation* demonstrates an effective way for heuristic approximation. To follow this elegant approximation, a bi-sectioning based dual operation (Du et al., 2010) approach is utilized. That is: from the sample points an initial TIN surface is constructed, we compute its dual mesh and take the space tessellation as approximated Voronoi cells; the approximated Voronoi tessellation is then optimized within the cCVT iteration. But different to clustering approach, we use each approximated Voronoi cell to (vertically) clip the original dense DEM surface, called referring patch. By this exactly clipped referring patch we compute accurate energy estimation for new approximated sites. The global clipping computation is localized using a *kd-tree* structure.

The localization and accurate referring energy computation makes cCVT iteration converge fast. The efficiency of the cCVT approximation as a whole is comparable to that of the elegant clustering approach. We go no further for the complexity analysis but however provide an implementation of the classical clustering with the same settings as the cCVT in the attachment. The pseudo-code of this improved cCVT iteration is described as follows:

Algorithm2 cCVT_iteration

Input: vertices $\boldsymbol{N} = \{\boldsymbol{v_i}\}_{\boldsymbol{k}}^{\boldsymbol{1}}$, *scale transformation* ***Ratio***.

1) Construct the original DEM surface ***oriPd*** *from vertices* ***N****, compute density function* $\boldsymbol{\rho}$ *based on robust mean curvature estimation;*

2) Extract and mark boundary points ***B****, mark stationary control points, check points as* ***C****, extract and mark the feature points* ***F****;*

3) Perform constrained Delaunay triangulation on point set ***{B, C, F}****, with boundary* ***{B}*** *and structural terrain features* ***{C}*** *as constraints; obtain an initial approximated* ***TIN*** *surface;*

4) While ($\Delta \boldsymbol{E} > \boldsymbol{Threshold}$*)*

{

4.1) Compute ***TIN****'s dual* ***TD****;*

4.2) For the ***n*** *vertices* $\boldsymbol{r_j}$ *in* ***TD****, extract its direct incident facets as* $\boldsymbol{FS} = \{\boldsymbol{T_i}\}_{\boldsymbol{n}}^{\boldsymbol{1}}$*;*

4.3) For each $\boldsymbol{T_j}$ *in* ***FS***

{

4.3.1) Compute its minimal bounding box ***BBox$_j$****, fast compute its intersection of* ***oriPd*** *using an kd-tree, obtain a narrowed reference geometry* ***narrPd****;*

4.3.2) Compute exact intersection of ***T$_j$*** *and* ***narrPd****, push the result into reference sets* ***REF={ref$_j$}****;*

}

4.4) For each ***ref$_j$*** *in* ***REF***

{

4.4.1) Compute approximated Voronoi barycentre: $\overline{\boldsymbol{x}} = \frac{\sum \boldsymbol{\rho \cdot x \cdot area(ref_j)}}{\sum \boldsymbol{\rho \cdot area(ref_j)}}$; $\overline{\boldsymbol{y}} = \frac{\sum \boldsymbol{\rho \cdot y \cdot area(ref_j)}}{\sum \boldsymbol{\rho \cdot area(ref_j)}}$; $\overline{\boldsymbol{z}} = \frac{\sum \boldsymbol{\rho \cdot z \cdot area(ref_j)}}{\sum \boldsymbol{\rho \cdot area(ref_j)}}$;

4.4.2) Use kt-tree for fast intersection computation of point $(\overline{\boldsymbol{x}}, \overline{\boldsymbol{y}}, \overline{\boldsymbol{z}})$ *and* ***oriPd****, with the result used as the projected nearest point; push it into the new candidate point set* ***F'****;*

}

4.5) Using ***{B, C}*** *as constraints, Delaunay triangulate point set* ***{B, C, F'}*** *and obtain reconstructed* ***TIN'****;*

4.6) Compute ***E*** *on* ***TIN'****;*

}

Here, we illustrate this algorithm by using a numerical mountain model. The analytic equation is:

$$z = (4x^2 + y^2) \cdot e^{-x^2-y^2}\ , \tag{5}$$

It has two peaks, two saddles and a pit. We rasterize it with a 49×49=2401 regular grid (Figure **1**, left). As for effectiveness, we set the transformation scale at 0.1 (***Ratio*** = 0.1), that is, there are about 240 points left. The sample set includes 56 boundary points, 5 critical points, and an additional 169 random points for visual saturation purposes (Figure **1**, left; the red points are randomly generated points, the blue points are boundaries, and the green points are critical points). Relief feature points are always abundant in a real terrain dataset, so additional random points are rarely needed. A robust mean curvature estimation is computed on the original high-resolution surface ***oriPd*** (Figure **1**, right), by which we can clearly distinguish critical points as peaks, saddles, and pits. The initially approximated TIN surface from the sample set is shown in Figure **2** (left), and its generated dual mesh is shown in Figure **2** (right), which corresponds to step 3 of Algorithm2. Figure 3 shows the dual cell of sample points, which is the key idea of the cCVT approximation. Figure 4 and Figure 5 shows the algorithm steps 4.3.1 and 4.3.2, respectively, where the exact clipping is completed on the original DEM surface. Figure 6 and Figure 7 show the final computation on the reference patch of the first sample point, which corresponds to the algorithm steps 4.4.1 and 4.4.2. Figure **8** exhibits the result of the first iteration compared to that of the final iteration, with the initial sample points included (top). A comparison of the constructed approximate TIN grids of the initial state and final state is illustrated in the middle, while the curvature distribution that represents the terrain feature comparison is illustrated at the bottom.

The results show how the embedded stationary points (control points and boundary points), feature points, and random points are spatially equalized (Figure **8**). Additionally, the cCVT generated a variable-resolution terrain grid (middle right); the convergent TIN grid exhibited nearly uniform high quality, and the convergence process generally resembled *Lloyd's Relaxation* (Figure 9).

Notably, the direct reference on the original DEM surface is realized by the exact geometry clipping, which linearly interpolated the high-resolution surface literally. This clipping technique has several important benefits: it guarantees accurate energy estimation, it avoids the generation of invalid clustering cells or zigzagging cells, and it promises exact site position calculation which will warrants improved grid quality.

3 Multiresolution DEM Experiments

3.1 Experimental datasets

Two sites with significant geomorphological characteristics were selected. Experimental site 1 is Mount St. Helens, located in Skamania County, W.A., USA. This mountain is an active volcano whose last eruption occurred in May, 1980, and deep magma chambers have been observed recently (Hand, 2015). This site was selected for its typical mountain morphology along cone ridges and evident fluvial features downhill, where heavy pyroclastic materials and deposits are present. These two distinctively different terrain structures mingle together, posing challenges for DEM generalisation.

The St. Helens dataset was selected from Puget Sound LiDAR (http://wagda.lib.washington.edu/data/type/elevation/lidar/st_helens/), this LiDAR dataset was collected in late 2002. The selected dataset is a 2924×3894 regular grid with a 3 m cell size and covers an area of approximately 102 km^2. The elevation ranges from 855.32 to 2539.34 m. The image and hillshade views of these data are illustrated in Figure **10**.

Experimental site 2 is the Columbia Plateau, USA. This area has been labelled as UTM zone 11, we hereafter call it UTM11 (http://gis.ess.washington.edu/data/raster/tenmeter/), this LiDAR dataset was collected in 2009. The selected site is located on the border of Columbia County and Walla Walla County, WA. The south-eastern corner is located in the Wenaha-Tucannon Wilderness, Umatilla National Forest. This area contains rugged basaltic ridges with steep canyon slopes at high elevations (average of 1700 m). The north-western area is located near Dayton City, which is a vast agricultural and ranching area with relatively smoother morphology at low elevations (averagely 500 m). This site is selected for the coexistence of these two prominent different surface morphology. That is, if the generalisation scheme emphasizes the high elevation areas with sharp variation, the surface interpolation as a whole might be unbalanced, which may result in smoothing the low elevation areas.

The selected UTM11 dataset is a 3875 × 3758 grid with a 10 m cell size and covers an area over 1456 km^2. The elevation ranges from 3533 to19340 cm. The image and hillshade views of these data are shown in Figure **11**.

3.2 Comparison method

As aforementioned, DEM generalisation has long been studied in geoscience, with numerous methods proposed over time. One of the most classical approaches is the hierarchical insertion (or decimation) of feature points to construct a TIN grid under a destination scale. This type of heuristic feature point refinement (HFPR) performs very well in terms of surface

approximation and terrain structure retention. For this reason, although HFPR methods generally cannot guarantee high-quality grids, these methods are suitable for comparison purposes.

A typical HFPR starts with four corner points from a dense DEM image and constructs a Delaunay triangular grid that contains two triangles. The rest of the points are weighted by their distance to the triangular surface or other error criteria and queued. The point with the largest priority in the queue is selected, and the grid is modified by using incremental Delaunay triangulation. This process loops until some error threshold is satisfied (Heckbert and Garland, 1997). Michael Garland provided a classical HFPR implementation (http://mgarland.org/software.html), and many other variants are available in GIS, meshing, and visualisation tool suites.

3.3 Quantitative comparisons

We performed the processes from Algorithm2 for the two experimental datasets, including triangulation and curvature estimation, boundary point extraction and marking, feature point extraction based on curvature significance and marking, optimization loop through cCVT, etc. For effectiveness, the transformation ***Ratio*** was set to range from 5% to 0.1% points density (comparable to the 3.1% to 0.6% setting in (Zhou and Chen, 2011)).

The accuracy of the surface approximation determines the final surface interpolation precision and is thus a basic quality comparison index. Here we applied a statistical interpolation method to measure the surface approximation precision. From each triangle on the cCVT-generated quasi-uniform TIN grid, a random point is selected and a vertical line is introduced, to intersect the original dense DEM surface and the HFPR generalised TIN at the same time. Error estimation of the surface approximation could be obtained from these intersection points. We computed the mean error, maximum error, and root mean squared error (RMSE) for this elevation interpolation (TIN interpolation); the results are listed in Table 1. Furthermore, we computed the aspect ratios of the triangles for both generalised TIN surfaces to measure the grid quality, which are also listed in Table 1. RMSEs with varied transformation ***Ratios*** are listed in independent rows and columns in Table 1.

From the results in the Table 1 we can conclude that hat, under the same resolution (point density), transformed DEM surface from cCVT method is generally more precise than that from HFPR method. While all surface approximation precision (compared to the original) decrease as the resolution coarsened.

3.4 Qualitative comparison

A qualitative index is usually measured from terrain structure retention aspects. According to the result TINs from the two experimental datesets, both the cCVT and HFPR methods performed well from visual examination. However, upon closer inspection, the surface generated by cCVT has a smoother transition effect than that from HFPR (**Figure 12**). HFPR accumulated more samples around sharp features (c.f. Figure **13**), its surface exhibited clearer impression because flat details were smoothed out. From a visual examination, it may be concluded that, under the same transformation conditions, HFPRs may exert a stronger generalisation effect than cCVTs.

However, a stronger generalisation effect actually decreases the general approximation's precision, which may result in structural distortion or misconfiguration. Figure **14** illustrates a closer examination of St. Helens. Some structural details on the original surface were recovered by the cCVTs but not by the HFPRs. This terrain structure loss occurred on both smooth areas and steep areas, as illustrated in Figure **14**. Figure **15** illustrates similar structural detail loss from HFPRs in the UTM11 dataset.

Terrain structural features could also be measured from DEM derivatives such as the slope, aspect, hydrological structural lines, etc. Here, we used contours to compare the generalisation accuracy using experimental site 2. Upon the same configurations (80 m elevation increments), we generated contours for the original dense TIN (rendered in red), the cCVT-generated TIN (rendered in blue), and the HFPR-generated TIN (rendered in black) and overlapped the three sets of contours for comparison (Figure **16**). The illustrations demonstrate that, in most cases (Figure **16** b, c), the contours from the cCVT-generalised surface are more accurately conformed with those from the original dense surface, while the contours from the HFPR-generalised surface generally did not, except for some cases on steeper areas with sharp curvature variations (Figure **16** d). This result can be explained by the HFPR's stronger accumulation of sample points to sharp features, which guaranteed an edging out, if we noticed that the inspection area **d** is much smaller than **b** or **c**.

4 Disscussion

Topography transformation of DEM surfaces has been a deeply studied topic in geoscience, simplification techniques and generalisation principles are widely realised and adopted. Extracting terrain feature points and using these points to construct a generalised surface is one successful approach, which may be owned to the feature points' strong capability on capturing terrain structures. However, TIN grids that are constructed purely from feature points may not be best approximated to original high-resolution surfaces. Taking the mountain equation in Figure **1** for example, it has at least two peaks, two saddles, and one pit close to zero level. Presume scale transformation requires that only two critical points are left; selecting both peak points is more reasonable than selecting the pit point, even if the pit point has a stronger quantitative index (curvature in this case) than those of the peak points. This observation implies that, if global surface interpolation precision are more importantly demanded, robust approach like cCVT that incorporates surface approximation and terrain feature retention should be considered.

Among those classical DEM generalisation approaches, heuristic feature point refinement (here refinement is a method description opposed to decimation, rather than a mesh enhancement strategy) is an outstanding example. As illustrated by Table 1, Figure **12**, and Figure **16**, HFPR methods perform excellently in terms of surface approximation and surface morphology retention. On the treatment of feature points, these methods use a heuristics strategy by introducing incremental Delaunay triangulation, which considers the point with the largest error from the constructed TIN. However, the impact of the feature point being-inserted on the feature points have-inserted is not considered because computational burden. As a result, feature points may cluster around relief with sharp variations, as exemplified by Figure **12**. Too many feature points

accumulating near sharp features means that relatively scarce of feature points are present in flat areas, which would eventually lead to terrain structure distortion or misconfiguration, as shown in Figure **14**, Figure **15**, and Figure **16**. Sometimes, this type of structural loss is unbearable. For example, the terrain relief at high elevations under the studied scale (10 m cell spacing) in experimental site 2 indicated a fiercer landform than at lower elevations. The accumulation of too many sample points in high-elevation areas may result in the distortion of the smooth anthropogenic terrain morphology in low-elevation areas.

cCVT starts by constructing a terrain-adaptive multiresolution grid. The iterations use a robust mean curvature as a density function which is based on the curvature's capability to characterise shapes and conduct shape evolution. CVT is essentially a two-stepped optimization loop (c.f. Algorithm1 in Section 2.2). The process of spatially equalising feature points has been seldom considered by classical approaches, which may explain why cCVT generally prevails over HFPRs (c.f. Table 1).

On the other hand, CVT is an approach within variational framework. The result from iteration relies on the boundary conditions and initial conditions. Hence, this article employed a feature point scheme (with additional input points considered) as a relatively stationary initial condition to maintain algorithm stability. The requirement of embedding feature points of interest, along with consideration to avoid the problematic *k-means* like clustering, prompt us to develop a non-clustering approach with an exact energy referring method. Experiments on ten million DEM points demonstrated that the exact clipping approach performed comparably to the elegant clustering approach. Notably, the triangles from the cCVT-generated TIN surface exhibited a maximum aspect ratio that was less than 5.0 (c.f. Table 1), which implies that the build-up terrain grid satisfied the numerical stability requirement from classical finite element or finite volume computations.

5 Conclusions

In this article, a high-fidelity multiresolution DEM model was proposed for scale transformation. Multiresolution models are an essential tool to incorporate more scales. A high-fidelity generalised DEM model can build a concrete topographic layer from which fine endogenous or exogenous processes can be assessed under proper scale conditions. These two aspects were achieved by our devised curvature-based CVT. cCVT optimization increases the precision of surface approximations compared to existing heuristic DEM generalisations, while the equalisation of feature points from both the spatial domain and curvature magnitude domain (i.e., frequency domain) facilitates multiresolution and high-fidelity approximations.

Evaluation of cCVT multiresolution DEM model on Earth and environmental systems in wide-ranged domains and scales is needed in further study. Considering the Earth system situation of global modeling tyranny (Ringler et al., 2011), this may imply a consideration of curvature of the Earth itself into the cCVT model.

Code Availability

The main cCVT algorithm and the classical k-means clustering CVT implementation, which has the same building environment as the cCVT, are provided. However, some source codes from the third parties were used in our research, and we do not have the rights to re-deploy these source codes. Please contact the corresponding author for the complete source code.

Acknowledgement

This study is funded by the Special Fund for Surveying, Mapping and Geo-information Scientific Research in the Public Interest (201412014), the National Natural Science Fund of China (41271453) and Scientific and Technological Leading Talent Fund of National Administration of Surveying, mapping and geo-information (2014).

References

Aguilar, F. J., Agüera, F., Aguilar, M. A., and Carvajal, F.: Effects of Terrain Morphology, Sampling Density, and Interpolation Methods on Grid DEM Accuracy, Photogrammetric Engineering & Remote Sensing, 71, 805-816, 2005, doi: http://dx.doi.org/10.14358/PERS.71.7.805.

Ai, T. and Li, J.: A DEM generalization by minor valley branch detection and grid filling, ISPRS Journal of Photogrammetry and Remote Sensing, 65, 198-207, 2010, doi:10.1016/j.isprsjprs.2009.11.001.

Banchoff, T.: Critical points and curvature for embedded polyhedra, Journal of Differential Geometry, 1967. 1967, doi: 10.2307/2317380.

Bates, P. D.: Integrating remote sensing data with flood inundation models: how far have we got?, Hydrological Processes, 26, 2515-2521, 2012, doi: 10.1002/hyp.9374..

Bilskie, M. V., Coggin, D., Hagen, S. C., and Medeiros, S. C.: Terrain-driven unstructured mesh development through semi-automatic vertical feature extraction, Advances in Water Resources, 86, Part A, 102-118, 2015, doi:10.1016/j.advwatres.2015.09.020..

Bilskie, M. V. and Hagen, S. C.: Topographic accuracy assessment of bare earth lidar-derived unstructured meshes, Advances in Water Resources, 52, 165-177, 2013, . doi:10.1016/j.advwatres.2012.09.003.

Brioude, J., Angevine, W. M., McKeen, S. A., and Hsie, E. Y.: Numerical uncertainty at mesoscale in a Lagrangian model in complex terrain, Geosci. Model Dev., 5, 1127-1136, 2012, doi:10.5194/gmd-5-1127-2012.

Budd, C. J., Russell, R. D., and Walsh, E.: The geometry of r-adaptive meshes generated using optimal transport methods, Journal of Computational Physics, 282, 113-137, 2015, doi:10.1016/j.jcp.2014.11.007.

Cabello, S., Fort, M., and Sellarès, J. A.: Higher-order Voronoi diagrams on triangulated surfaces, Information Processing Letters, 109, 440-445, 2009, doi:10.1016/j.ipl.2009.01.001.

Cea, L. and Bladé, E.: A simple and efficient unstructured finite volume scheme for solving the shallow water equations in overland flow applications, Water Resources Research, 51, 5464-5486, 2015, doi: 10.1002/2014WR016547.

Chen, C. and Li, Y.: An orthogonal least-square-based method for DEM generalization, International Journal of Geographical Information Science, 27, 154-167, 2012, doi:10.1080/13658816.2012.674136.

Chen, C., Li, Y., and Yue, T.: Surface modeling of DEMs based on a sequential adjustment method, International Journal of Geographical Information Science, 27, 1272-1291, 2012, doi:10.1080/13658816.2012.704037.

Chen, C., Yan, C., Cao, X., Guo, J., and Dai, H.: A greedy-based multiquadric method for LiDAR-derived ground data reduction, ISPRS Journal of Photogrammetry and Remote Sensing, 102, 110-121, 2015, doi:10.1016/j.isprsjprs.2015.01.012.

Chen, Y. and Zhou, Q.: A scale-adaptive DEM for multi-scale terrain analysis, International Journal of Geographical Information Science, 27, 1329-1348, 2012, doi:10.1080/13658816.2012.739690.

Cohen-Steiner, D., Alliez, P., and Desbrun, M.: Variational shape approximation, ACM Trans. Graph., 23, 905-914, 2004, doi:10.1145/1186562.1015817.
Du, Q., Faber, V., and Gunzburger, M.: Centroidal Voronoi Tessellations: Applications and Algorithms, SIAM Review, 41, 637-676, 1999, doi:10.1137/S0036144599352836.
Du, Q., Gunzburger, M. D., and Ju, L.: Constrained Centroidal Voronoi Tessellations for Surfaces, SIAM Journal on Scientific Computing, 24, 1488-1506, 2003, doi:10.1137/S1064827501391576.
Du, Q., Max, G., and Ju, L.: Advances in Studies and Applications of Centroidal Voronoi Tessellations, Numerical Mathematics: Theory, Methods & Applications, 3, 119-142, 2010, doi: 10.4208/nmtma.2010.32s.1.
Fiddes, J. and Gruber, S.: TopoSCALE v.1.0: downscaling gridded climate data in complex terrain, Geosci. Model Dev., 7, 387-405, 2014, doi:10.5194/gmd-7-387-2014.
Florinsky, I. and Pankratov, A.: Digital terrain modeling with the Chebyshev polynomials, arXiv preprint arXiv:1507.03960, 2015. 2015.
Glover, R. W.: Influence of Spatial Resolution and Treatment of Orography on GCM Estimates of the Surface Mass Balance of the Greenland Ice Sheet, Journal of Climate, 12, 551-563, 1999, doi:10.1175/1520-0442(1999)012<0551:IOSRAT>2.0.CO;2.
Guba, O., Taylor, M. A., Ullrich, P. A., Overfelt, J. R., and Levy, M. N.: The spectral element method (SEM) on variable-resolution grids: evaluating grid sensitivity and resolution-aware numerical viscosity, Geosci. Model Dev., 7, 2803-2816, 2014, doi:10.5194/gmd-7-2803-2014.
Guilbert, E., Gaffuri, J., and Jenny, B.: Terrain Generalisation. In: Abstracting Geographic Information in a Data Rich World, Burghardt, D., Duchêne, C., and Mackaness, W. (Eds.), Lecture Notes in Geoinformation and Cartography, Springer International Publishing, 2014.
Hand, E.: http://news.sciencemag.org/earth/2015/11/deep-magma-chambers-seen-beneath-mount-st-helens, last access: 6, Dec 2015.
Heckbert, P. S. and Garland, M.: Survey of polygonal surface simplification algorithms, DTIC Document, 1997.
Hughes, J. K., Ross, A. N., Vosper, S. B., Lock, A. P., and Jemmett-Smith, B. C.: Assessment of valley cold pools and clouds in a very high-resolution numerical weather prediction model, Geosci. Model Dev., 8, 3105-3117, 2015, doi:10.5194/gmd-8-3105-2015..
Hunter, N. M., Bates, P. D., Horritt, M. S., and Wilson, M. D.: Simple spatially-distributed models for predicting flood inundation: A review, Geomorphology, 90, 208-225, 2007, doi:10.1016/j.geomorph.2006.10.021.
Jenny, B., Jenny, H., and Hurni, L.: Terrain Generalization with Multi-scale Pyramids Constrained by Curvature, Cartography and Geographic Information Science, 38, 110-116, 2011, doi:10.1559/15230406382110.
Jiménez, P. A. and Dudhia, J.: On the Ability of the WRF Model to Reproduce the Surface Wind Direction over Complex Terrain, Journal of Applied Meteorology and Climatology, 52, 1610-1617, 2013, doi:10.1175/JAMC-D-12-0266.1.
Ke, Y., Leung, L. R., Huang, M., Coleman, A. M., Li, H., and Wigmosta, M. S.: Development of high resolution land surface parameters for the Community Land Model, Geosci. Model Dev., 5, 1341-1362, 2012, doi: 10.5194/gmdd-5-1435-2012.
Kennelly, P. J.: Terrain maps displaying hill-shading with curvature, Geomorphology, 102, 567-577, 2008, doi:10.1016/j.geomorph.2008.05.046.
Kesserwani, G. and Liang, Q.: Dynamically adaptive grid based discontinuous Galerkin shallow water model, Advances in Water Resources, 37, 23-39, 2012, doi:10.1016/j.advwatres.2011.11.006.
Kim, B., Sanders, B. F., Schubert, J. E., and Famiglietti, J. S.: Mesh type tradeoffs in 2D hydrodynamic modeling of flooding with a Godunov-based flow solver, Advances in Water Resources, 68, 42-61, 2014, doi: 10.1016/j.advwatres.2014.02.013.
Kimmel, R. and Sethian, J. A.: Computing geodesic paths on manifolds, Proc Natl Acad Sci USA, 95, 8431-8435, 1998.
Kumar, S. V., Peters-Lidard, C. D., Santanello, J., Harrison, K., Liu, Y., and Shaw, M.: Land surface Verification Toolkit (LVT) – a generalized framework for land surface model evaluation, Geosci. Model Dev., 5, 869-886, 2012, doi: 10.5194/gmd-5-869-2012.
Lee, J. A. Y.: Comparison of existing methods for building triangular irregular network, models of terrain from grid digital elevation models, International Journal of Geographical Information Systems, 5, 267-285, 1991, doi:10.1080/02693799108927855.
Leempoel, K., Parisod, C., Geiser, C., Daprà, L., Vittoz, P., and Joost, S.: Very high-resolution digital elevation models: are multi-scale derived variables ecologically relevant?, Methods in Ecology and Evolution, 6, 1373-1383, 2015,

doi:10.1111/2041-210X.12427.
Lloyd, S.: Least squares quantization in PCM, Information Theory, IEEE Transactions on, 28, 129-137, 1982, doi:10.1109/TIT.1982.1056489.
Meyer, M., Desbrun, M., Schröder, P., and Barr, A.: Discrete Differential-Geometry Operators for Triangulated 2-Manifolds. In: Visualization and Mathematics III, Hege, H.-C. and Polthier, K. (Eds.), Mathematics and Visualization, Springer Berlin Heidelberg, 2003, doi:10.1007/978-3-662-05105-4_2.
Milnor, J. W.: Morse theory, Princeton university press, 1963.
Mitášová, H. and Hofierka, J.: Interpolation by regularized spline with tension: II. Application to terrain modeling and surface geometry analysis, Mathematical Geology, 25, 657-669, 1993, doi:10.1007/BF00893172.
Nikolos, I. K. and Delis, A. I.: An unstructured node-centered finite volume scheme for shallow water flows with wet/dry fronts over complex topography, Computer Methods in Applied Mechanics and Engineering, 198, 3723-3750, 2009, doi:10.1016/j.cma.2009.08.006.
Nunalee, C. G., Horváth, Á., and Basu, S.: High-resolution numerical modeling of mesoscale island wakes and sensitivity to static topographic relief data, Geosci. Model Dev., 8, 2645-2653, 2015, doi:10.5194/gmdd-8-2973-2015.
Pan, H., Choi, Y.-K., Liu, Y., Hu, W., Du, Q., Polthier, K., Zhang, C., and Wang, W.: Robust modeling of constant mean curvature surfaces, ACM Trans. Graph., 31, 1-11, 2012, doi: 10.1145/2185520.2185581.
Ringler, T., Ju, L., and Gunzburger, M.: A multiresolution method for climate system modeling: application of spherical centroidal Voronoi tessellations, Ocean Dynamics, 58, 475-498, 2008, doi:10.1007/s10236-008-0157-2.
Ringler, T. D., Jacobsen, D., Gunzburger, M., Ju, L., Duda, M., and Skamarock, W.: Exploring a Multiresolution Modeling Approach within the Shallow-Water Equations, Monthly Weather Review, 139, 3348-3368, 2011, doi:10.1175/MWR-D-10-05049.1.
Schneider, B.: Extraction of Hierarchical Surface Networks from Bilinear Surface Patches, Geographical Analysis, 37, 244-263, 2005, doi: 10.1111/j.1538-4632.2005.00638.x.
Shi, W. Z., Li, Q. Q., and Zhu, C. Q.: Estimating the propagation error of DEM from higher‐order interpolation algorithms, International Journal of Remote Sensing, 26, 3069-3084, 2005, doi:10.1080/01431160500057905.
Tarolli, P.: High-resolution topography for understanding Earth surface processes: Opportunities and challenges, Geomorphology, 216, 295-312, 2014, doi:10.1016/j.geomorph.2014.03.008.
Valette, S. and Chassery, J.-M.: Approximated Centroidal Voronoi Diagrams for Uniform Polygonal Mesh Coarsening, Computer Graphics Forum, 23, 381-389, 2004, doi: 10.1111/j.1467-8659.2004.00769.x.
Valette, S., Chassery, J. M., and Prost, R.: Generic Remeshing of 3D Triangular Meshes with Metric-Dependent Discrete Voronoi Diagrams, Visualization and Computer Graphics, IEEE Transactions on, 14, 369-381, 2008, doi:10.1109/TVCG.2007.70430..
Weibel, R.: Models and Experiments for Adaptive Computer-Assisted Terrain Generalization, Cartography and Geographic Information Systems, 19, 133-153, 1992, doi:10.1559/152304092783762317.
Weller, H., Browne, P., Budd, C., and Cullen, M.: Mesh adaptation on the sphere using optimal transport and the numerical solution of a Monge–Ampère type equation, Journal of Computational Physics, 308, 102-123, 2016, doi:10.1016/j.jcp.2015.12.018.
Weller, H., Weller, H. G., and Fournier, A.: Voronoi, Delaunay, and Block-Structured Mesh Refinement for Solution of the Shallow-Water Equations on the Sphere, Monthly Weather Review, 137, 4208-4224, 2009, doi:10.1175/2009MWR2917.1 .
Wilby, R. L. and Wigley, T. M. L.: Downscaling general circulation model output: a review of methods and limitations, Progress in Physical Geography, 21, 530-548, 1997, doi:10.1177/030913339702100403.
Wilson, J. P.: Digital terrain modeling, Geomorphology, 137, 107-121, 2012, doi:10.1016/j.geomorph.2011.03.012.
Wilson, J. P. and Gallant, J. C.: Terrain Analysis: Principles and Applications. In: Digital Terrain Analysis, 2000.
Zakšek, K. and Podobnikar, T.: An effective DEM generalization with basic GIS operations, 8th ICA WORKSHOP on Generalisation and Multiple Representation. A Coruña, July, 2005.
Zarzycki, C. M., Jablonowski, C., and Taylor, M. A.: Using Variable-Resolution Meshes to Model Tropical Cyclones in the Community Atmosphere Model, Monthly Weather Review, 142, 1221-1239, 2014, doi:10.1175/MWR-D-13-00179.1.
Zhou, Q. and Chen, Y.: Generalization of DEM for terrain analysis using a compound method, ISPRS Journal of Photogrammetry and Remote Sensing, 66, 38-45, 2011, doi:10.1016/j.isprsjprs.2010.08.005.

Table 1 Quantitative comparison of the grid quality at scale transformation *Ratio* 1%

Dataset	Dense DEM Points	Random Interpolation Points	Approx. Method	Mean Error (m)	Max Error (m)	RMSE (m)	Max. Aspect Ratio
St. Helen 3 m	11,386,056	230,909	cCVT	0.0353	23.05	1.6145	3.23
			HFPR	0.1107	191.31	2.3714	9255
UTM11 10 m	14,562,250	301,255	cCVT	0.5773	37.70	3.77313	4.09
			HFPR	0.8765	487.81	6.71214	8426

Interpolated elevation RMSEs (m) at varied scale transformation *Ratios*

Dataset	Approx. Method	5%*	1%	0.5%	0.1%
St. Helens 3 m	cCVT	0.636	1.614	2.455	5.772
	HFPR	1.028	2.371	4.006	11.779
UTM11 10 m	cCVT	1.239	3.773	6.593	19.997
	HFPR	3.087	6.712	10.137	28.460

* The *Ratio* percent number means *n*% points left.

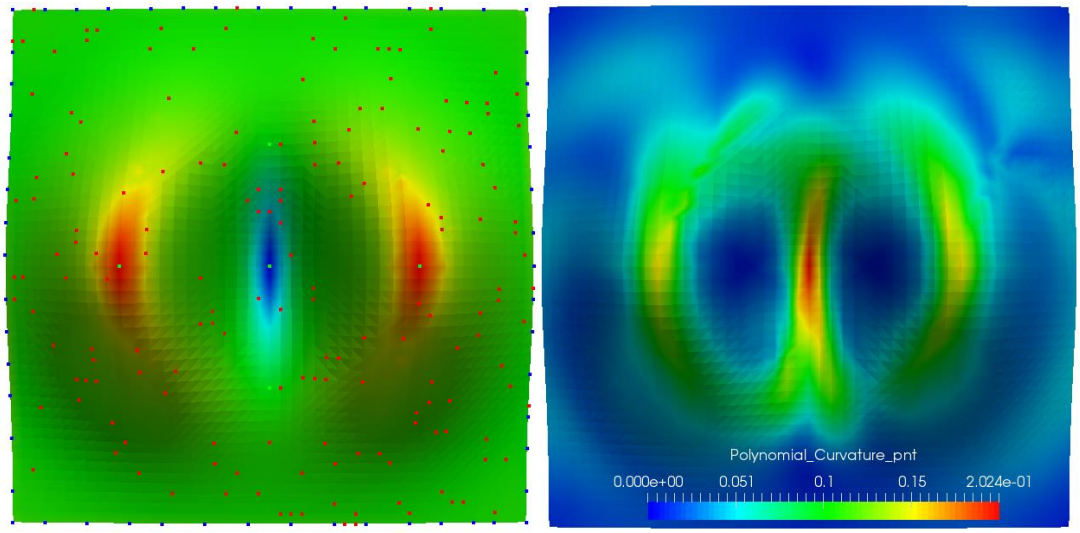

Figure 1 High-resolution grid of a mountain equation (5). Left: original grid *oriPd* in 49×49 resolution, rendered in mean curvature. The sample points were also rendered on oirPd; the blue points are boundary points, the green points are critical points, and the red points are random points. Right: robust mean curvature estimation. The saddle terrain features, peaks, and pits can be distinguished, compared to depicting on the left.

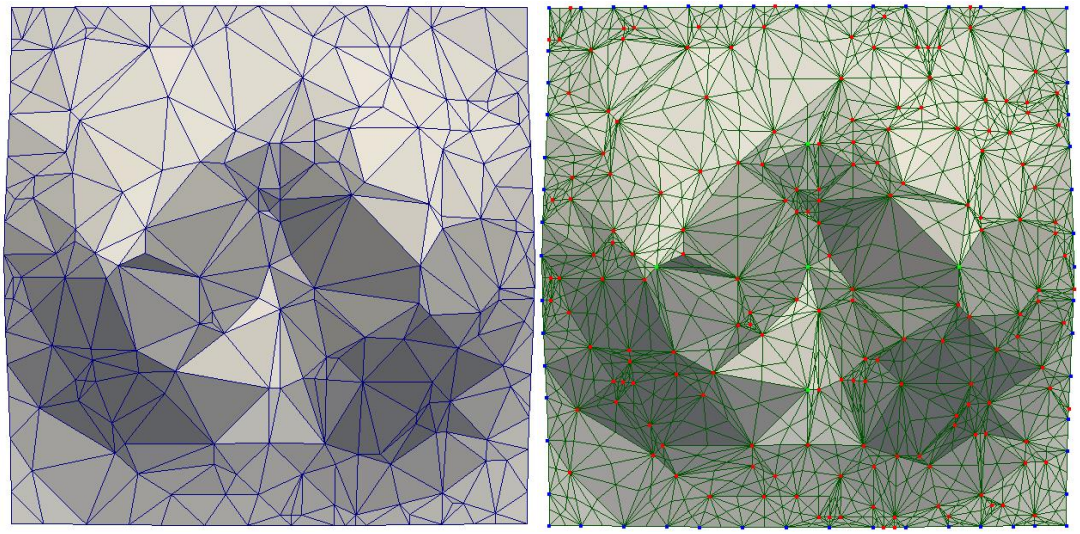

Figure 2 Initial *TIN* surface (left) and its dual grid *TD* (right). The initial sample points on the dual grid are also rendered.

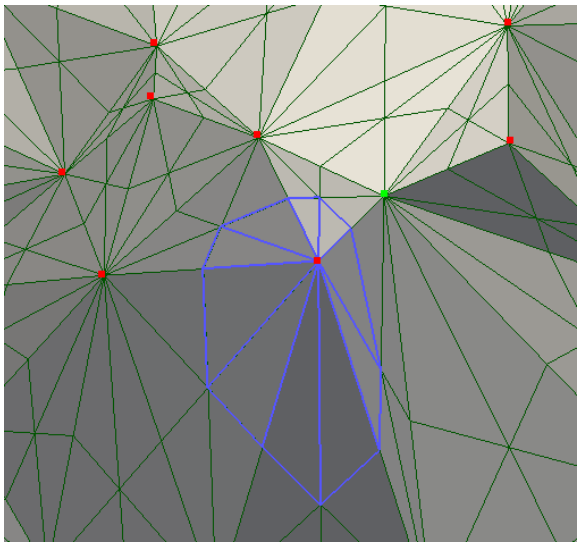

Figure 3 The incident triangles toward the first vertex r_i on the dual grid comprise an initial approximated Voronoi cell (rendered as a blue wireframe); the centre vertex is rendered in red.

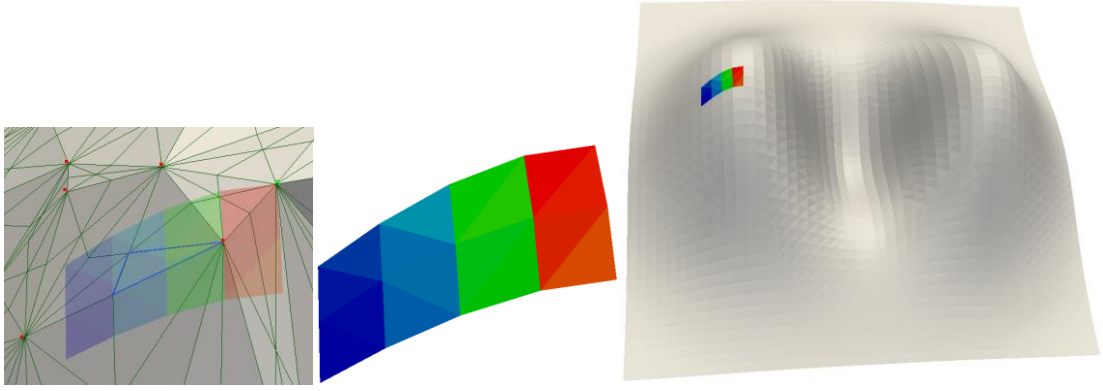

Figure 4 A triangle T_j (rendered in semi-transparent blue) with its minimal bounding box's intersection part *narrPd* with the original grid on the approximate grid (left), the localized intersection part *narrPd* alongside (middle), and the intersection part on the original grid *oriPd* (right).

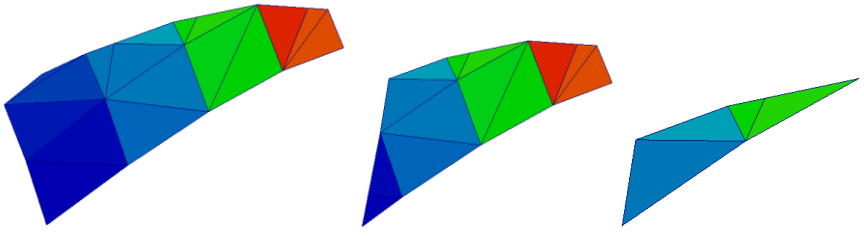

Figure 5 Exact clipping steps of *narrPd* with T_i. The sequence from left to right illustrates the edge clipped results.

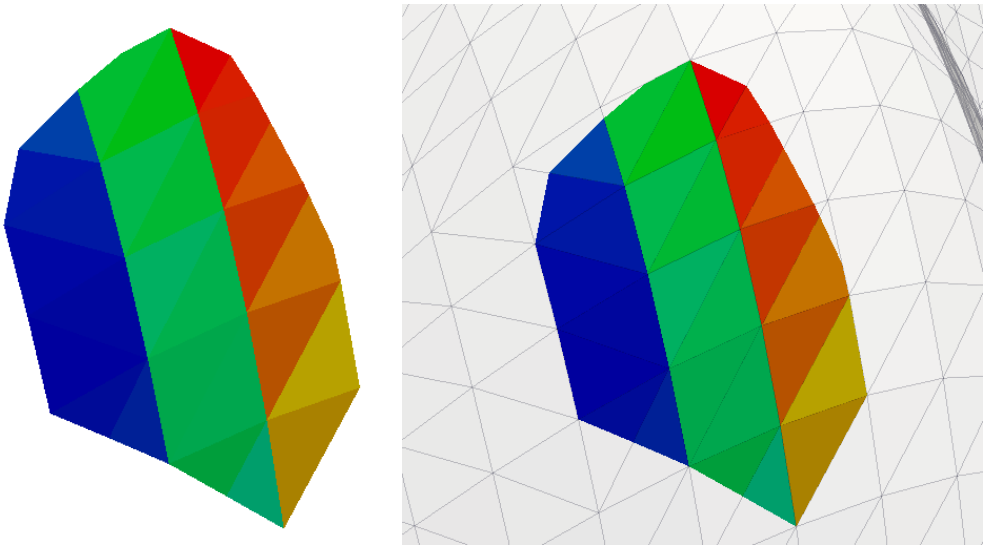

Figure 6 Reference patch ref_j on the original DEM surface of an initial Voronoi cell, with the centre at r_i (left). Right: ref_j on the original DEM surface *oriPd*.

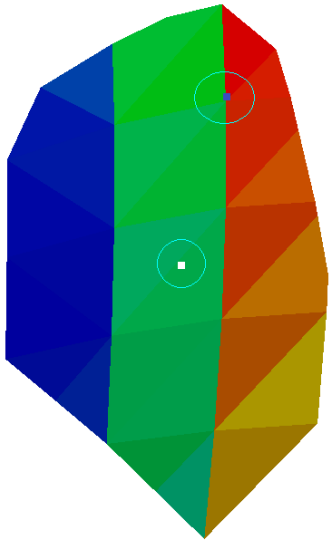

Figure 7 Barycentre computation based on the reference patch ref_j; the original site is the white block in the circle, the newly computed site and its projection on *oriPd* is depicted as blue block in the circle.

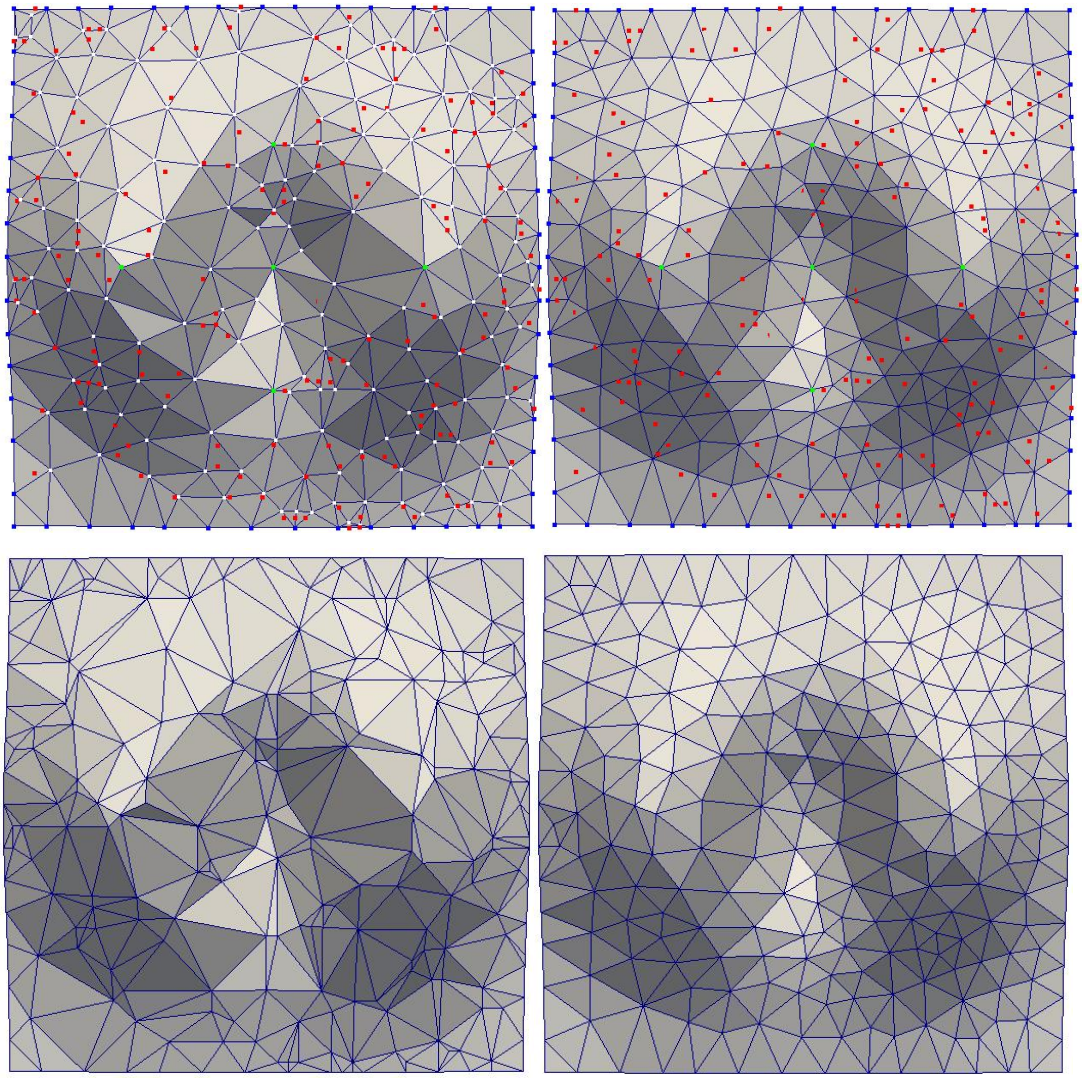

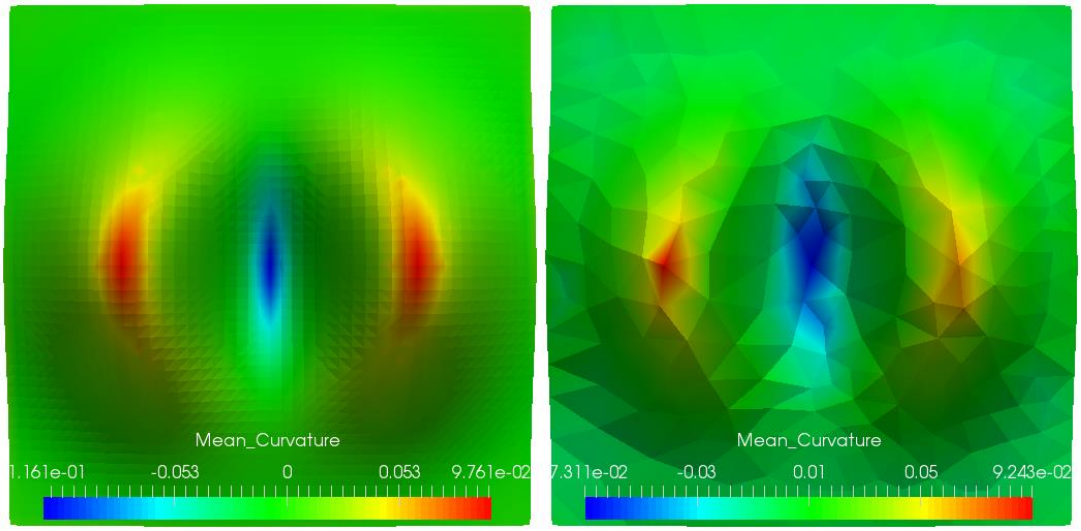

Figure 8 Converged results comparison. Top left: reconstructed TIN surface from one iteration with the initial points presented. Top right: the converged TIN surface with the initial sites, after about 140 loops. Middle: the initially approximated TIN surface (left) and the final TIN surface (right). Bottom: curvature distribution on the original surface (left) and the generalised grid (right).

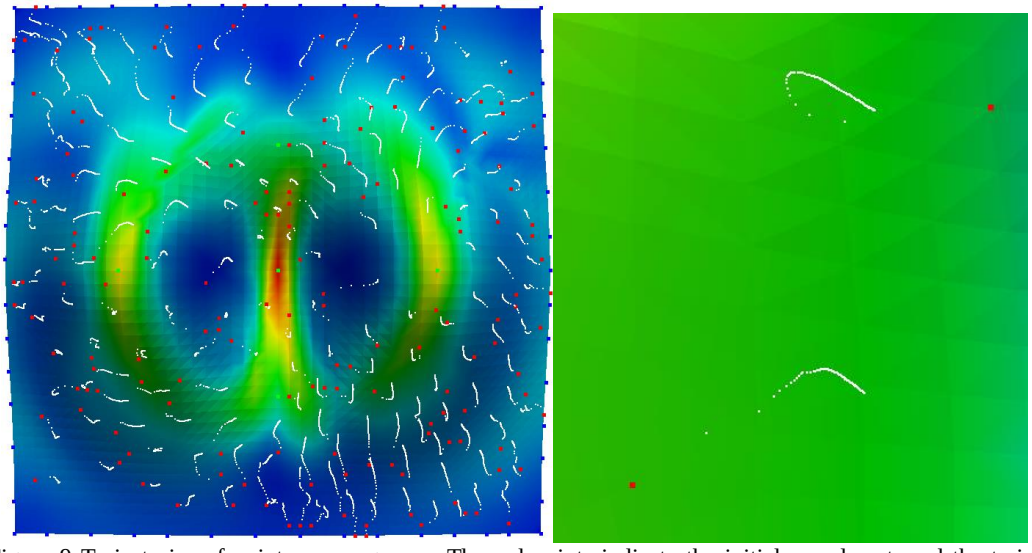

Figure 9 Trajectories of points convergences. The red points indicate the initial sample set, and the trajectories show the convergence trends, with closer gaps between candidate points. The right side shows a close view of the convergence of two points. These trends imply that the cCVT's convergence complies with *Lloyd Relaxation* linear convergence.

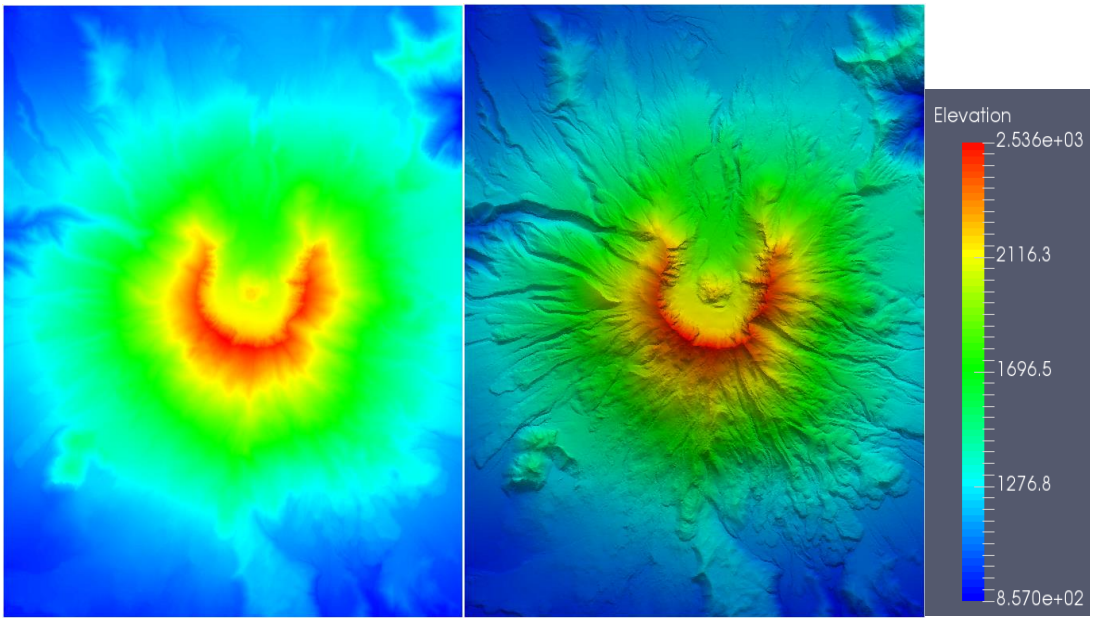

Figure 10 Experimental Site 1: Mount St. Helens. Left: image view. Middle: hillshade view. It is a 2924x3894 grid with a 3 m cell size.

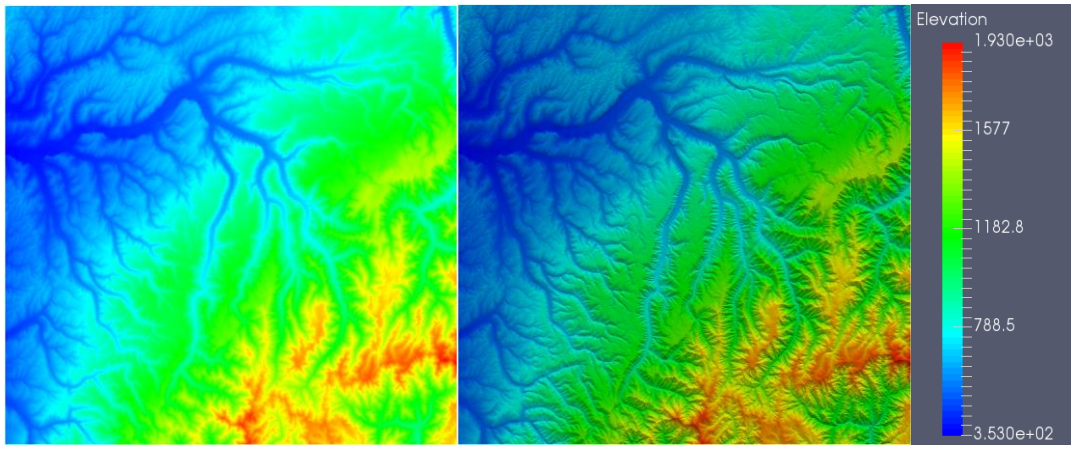

Figure 11 Experimental Site 2: UTM11 Zone. Left: image view. Middle: hillshade view. It is a 3875 x 3758 grid with a 10 m cell size.

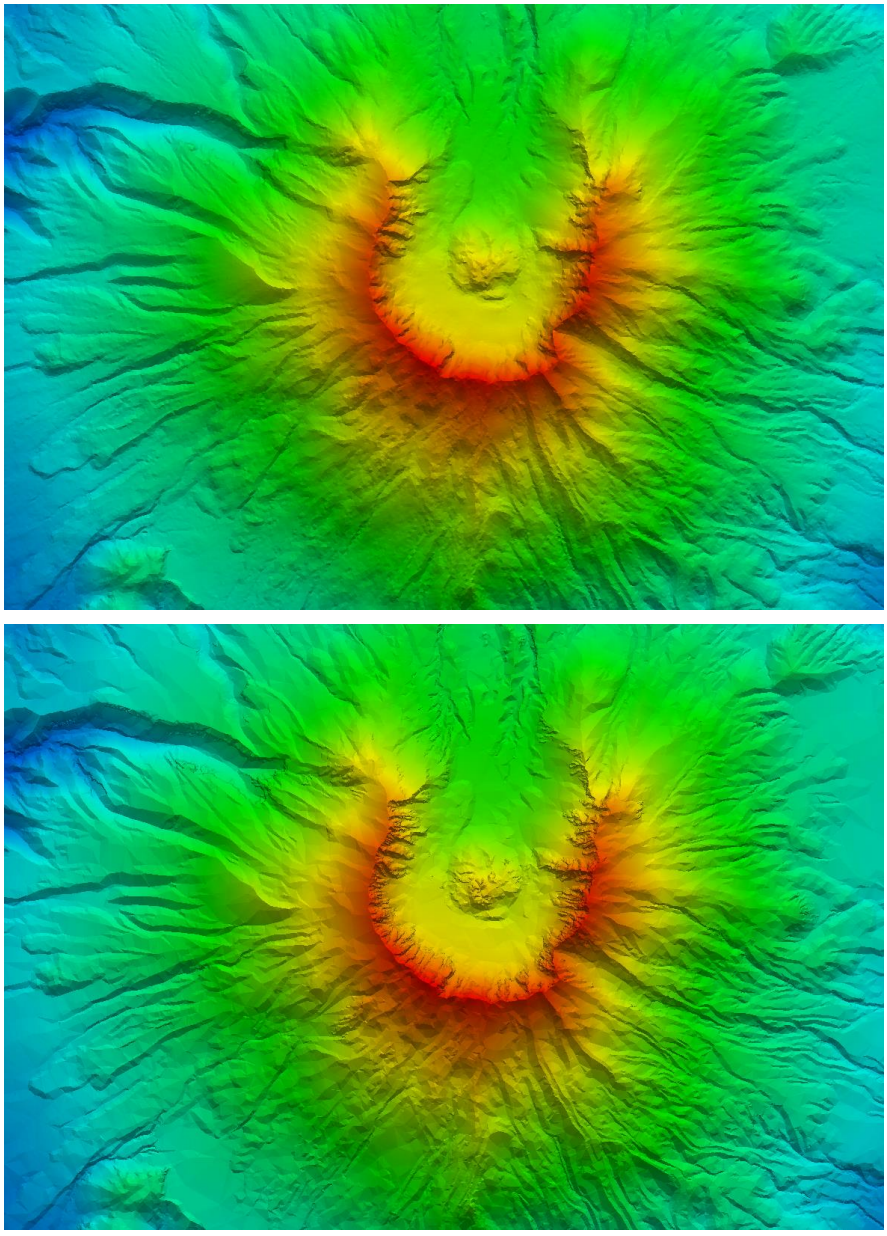

Figure 12 Visual examination of St. Helens. Top: cCVT grid. Bottom: HFPR grid. The latter grid appears more rigid than the former, which implies a stronger generalisation effect.

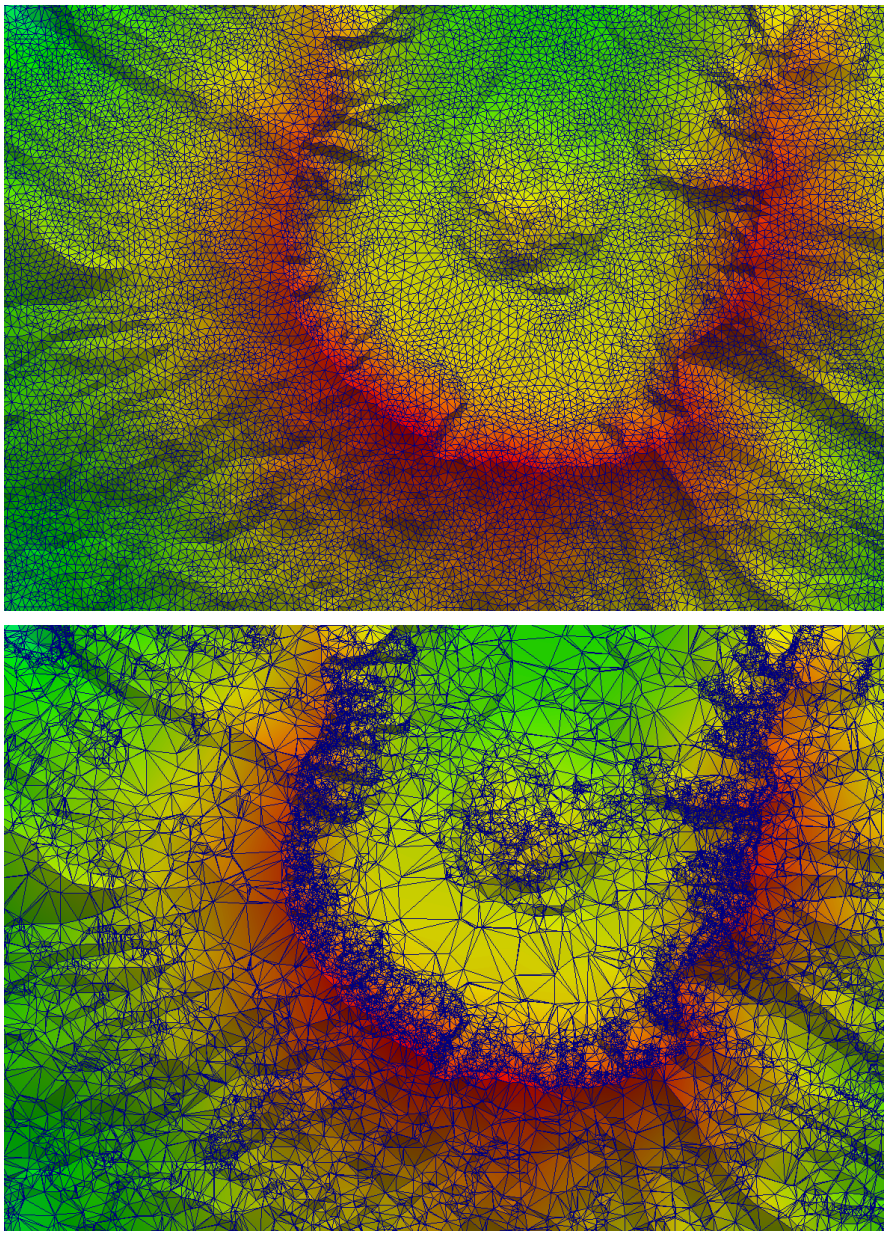

Figure 13 Grid quality from an intuitive comparison. Top: cCVT-generalised grid with nearly uniform triangles. Bottom: HFPR generalised grid with irregular triangles.

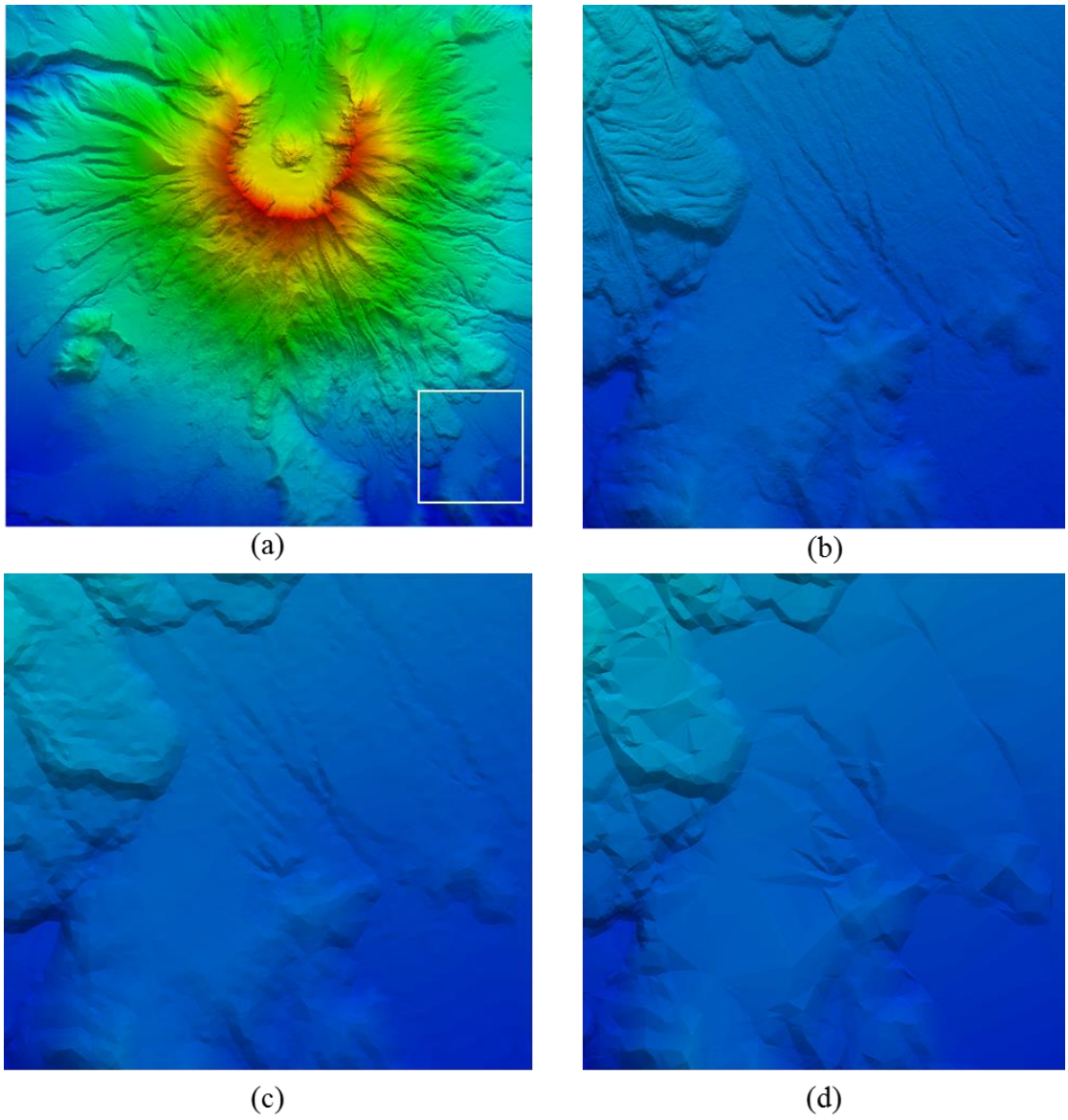

Figure 14 Detail loss of the HFPR generalisation grid. The inspected area in the experimental site is bounded by the white rectangle (a); the magnified inspection area on the original dense TIN (b); the area on the cCVT-generalised TIN (c); and the area on the HFPR-generalised TIN (d). From the close view it can be seen that the HFPR method generate a rougher grid than the CVTs. Thus, structural distortion or misconfiguration might be introduced.

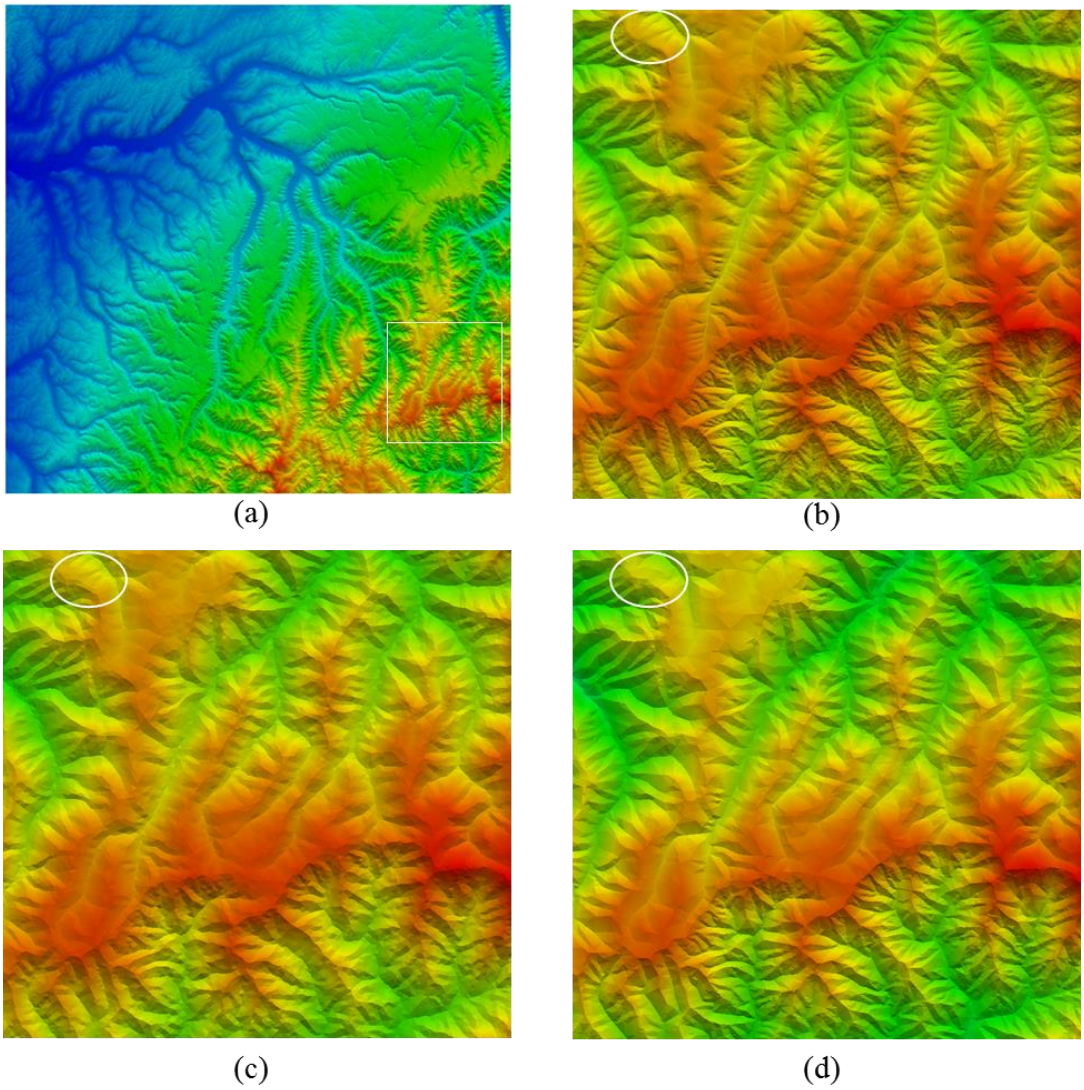

Figure 15 Detail loss from the HFPR method in the UTM11 dataset. (a) The inspection area in the entire experimental site. The magnified view of the inspection area is shown on the original dense DEM (b), on the cCVT-generalised TIN (c), and on the HFPR-generated TIN surface (d). The fold morphology in the white ellipse were recovered by the cCVT method but not by the HFPR method.

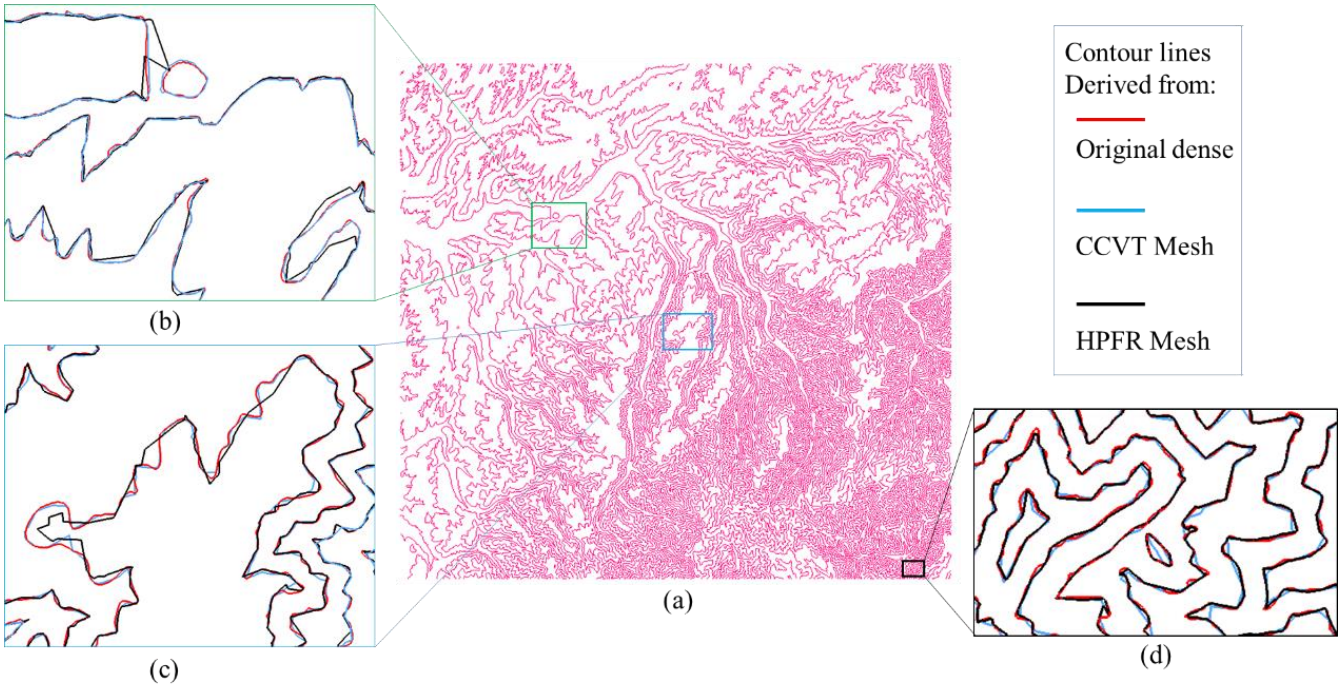

Figure 16 Comparison of the derived contour lines. The contours from the dense UTM11 dataset are shown in (a) and rendered in red. Three areas in the boxes were magnified to show the differences in the contours configuration. The blue contour lines are from the cCVT-generalised TIN surface, and the black lines are from the HFPR-generated TIN surface. According to the illustrations in (a) and (b), the contours that were derived from the cCVT grid (rendered in blue) are more in line with those from the original dense surface (rendered in red). The contours from the HFPR grid (rendered in black) may sometimes edge out on areas with steep slopes, as shown in (d), because HFPR method accumulated a relatively abundant sample points around these areas.